IVYSPRING INTERNATIONAL PUBLISHER

Theranostics

2018; 8(3): 785-799. doi: 10.7150/thno.21491

Research Paper

^{131}I-Labeled Copper Sulfide-Loaded Microspheres to Treat Hepatic Tumors via Hepatic Artery Embolization

Qiufang Liu[1, 3, 8*], Yuyi Qian[2*], Panli Li[1, 3, 8*], Sihang Zhang[2], Jianjun Liu[1, 8], Xiaoguang Sun[1, 8], Michael Fulham[3, 6, 7], Dagan Feng[3, 7], Gang Huang[1, 3, 5, 8✉], Wei Lu[2, 4✉] and Shaoli Song[1, 3, 8✉]

1. Department of Nuclear Medicine, Ren Ji Hospital, School of Medicine, Shanghai Jiao Tong University, Shanghai, China;
2. Department of Pharmaceutics, School of Pharmacy, Key Laboratory of Smart Drug Delivery, Ministry of Education & State Key Laboratory of Molecular Engineering of Polymers, Fudan University, Shanghai, China;
3. SJTU-USYD Joint Research Alliance for Translational Medicine, Shanghai Jiao Tong University, Shanghai, China;
4. Department of Biomedical and Pharmaceutical Sciences, College of Pharmacy, The University of Rhode Island, Kingston, Rhode Island, United States;
5. Shanghai Key Laboratory for Molecular Imaging, Shanghai University of Medicine and Health Sciences, Shanghai, China;
6. Department of Molecular Imaging, Royal Prince Alfred Hospital, Australia and Sydney Medical School, University of Sydney, Sydney, Australia;
7. Biomedical and Multimedia Information Technology Research Group, School of Information Technologies, University of Sydney, Sydney, Australia;
8. Institute of Clinical Nuclear Medicine, Ren Ji Hospital, School of Medicine, Shanghai Jiao Tong University, Shanghai, China.

* Equal contribution

✉ Corresponding authors: Shaoli Song, M.D., Department of Nuclear Medicine, Ren Ji Hospital, School of Medicine, Shanghai Jiao Tong University, Shanghai 200127, China. Phone: +86-21-68383097; E-mail: shaoli-song@163.com. Wei Lu, Ph.D., Department of Pharmaceutics, School of Pharmacy, Key Laboratory of Smart Drug Delivery, Ministry of Education & State Key Laboratory of Molecular Engineering of Polymers, Fudan University, Shanghai 201203, China. Phone: +86-21-51980185; E-mail: wlu@fudan.edu.cn. Gang Huang, M.D., Department of Nuclear Medicine, Ren Ji Hospital, School of Medicine, Shanghai Jiao Tong University, Shanghai 200127, China. Phone: +86-21-68383850; E-mail: huang2802@163.com

Received: 2017.06.16; Accepted: 2017.11.15; Published: 2018.01.01

Abstract

Purpose: Transcatheter hepatic artery embolization therapy is a minimally invasive alternative for treating inoperable liver cancer but recurrence is frequent. Multifunctional agents, however, offer an opportunity for tumor eradication. In this study, we were aim to synthesized poly (lactic-co-glycolic acid) (PLGA) microspheres encapsulating hollow CuS nanoparticles (HCuSNPs) and paclitaxel (PTX) that were then labeled with radioiodine-131 (^{131}I) to produce ^{131}I-HCuSNPs-MS-PTX. This compound combines the multi-theranostic properties of chemotherapy, radiotherapy and photothermal therapy. In addition, it can also be imaged with single photon emission computed tomography (SPECT) imaging and photoacoustic imaging.

Methods: We investigated the value of therapeutic and imaging of ^{131}I-HCuSNPs-MS-PTX in rats bearing Walker-256 tumor transplanted in the liver. After the intra-arterial (IA) injection of ^{131}I-HCuSNPs-MS-PTX, ^{18}F-Fluorodeoxyglucose (^{18}F-FDG) micro-positron emission tomography/computed tomography (micro-PET/CT) imaging was used to monitor the therapeutic effect. PET/CT findings were verified by immunohistochemical analysis. SPECT/CT and photoacoustic imaging were performed to demonstrate the distribution of ^{131}I-HCuSNPs-MS-PTX *in vivo*.

Results: We found that embolization therapy in combination with chemotherapy, radiotherapy and photothermal therapy offered by ^{131}I-HCuSNPs-MS-PTX completely ablated the transplanted hepatic tumors at a relatively low dose. In comparison, embolization monotherapy or combination with one or two other therapies had less effective anti-tumor efficacy. The combination of SPECT/CT and photoacoustic imaging effectively confirmed microsphere delivery to the targeted tumors *in vivo* and guided the near-infrared laser irradiation.

Conclusion: Our study suggests that there is a clinical theranostic potential for imaging-guided arterial embolization with ^{131}I-HCuSNPs-MS-PTX for the treatment of liver tumors.

Key words: ^{131}I-hollow copper sulfide nanoparticles-microsphere-paclitaxel (^{131}I-HCuSNPs-MS-PTX), multifunctional, positron emission tomography/computed tomography (PET/CT), embolization.

Introduction

Liver cancer is the sixth most common cancer and the third leading cause of cancer-related mortality worldwide [1]. Across metastatic disease, liver metastases are seen in 25% of cases [2]. Clinically, only a small number of patients (9-27%) have the opportunity for surgery [3]. The standard approaches to liver cancer include surgical resection, liver transplantation and locoregional therapies including radiofrequency ablation (RFA), transarterial chemoembolization (TACE) and percutaneous ethanol injection (PEI) [4, 5]. The rate of tumor recurrence, however, following RFA or PEI is high [6, 7]. Some investigators have reported that combined locoregional therapy using RFA with TACE improves outcomes when compared to RFA alone [8, 9].

Conventional TACE (cTACE) usually consists of the intra-arterial (IA) infusion of a chemotherapeutic agent mixed with lipiodol and then embolic particles. Lipiodol has poor control over drug release [10]. Recently several investigators have shown that unlike the rapid release of the drug from lipiodol in cTACE, drug-eluting beads (DEB)-TACE can release drugs in a controlled and sustained way [11-13]. DEB-TACE has some limitations: a) there is a lack of imaging feedback to allow direct and precise delivery of the therapeutic agents to the target site [14]; b) current materials are mostly non-biodegradable, which can make repeat treatment for tumor recurrence problematic. Chemotherapeutic/embolic agents with imaging and therapeutic capabilities would overcome the limitations of cTACE and DEB-TACE, and perhaps provide greater treatment efficacy.

Recently, several nano/micrometer-sized materials have been developed that can serve as embolic and drug-delivery agents with high tumor uptake after IA injection and less potential damage to surrounding tissues [15, 16]. In addition, nanomaterials with intense photothermal coupling effects have been identified for near-infrared (NIR) laser-induced photothermal therapy (PTT) of tumors in preclinical studies [17-19]. Moreover, these nanoparticles are versatile with the ability to cater for diagnosis and therapy with temporally- and spatially-controlled drug delivery [20, 21], photoacoustic imaging [22, 23], and nuclear medicine imaging and therapy [24, 25]. Semiconductor CuS nanoparticles are a new class of photothermal coupling agents. The NIR absorption by CuS nanoparticles is derived from the *d*–*d* transition of Cu^{2+} ions, which is not affected by the solvent or the surrounding environment [26, 27]. The hollow CuS nanoparticles (HCuSNPs) have controlled drug release [28] and are suitable for photoacoustic imaging [29, 30]. ^{64}Cu-labeled CuS nanoparticles have been pre-clinically applied to positron emission tomography–computed tomography (PET/CT) imaging [31, 32] and radiotherapy [33]. Unlike gold nanostructures that are non-biodegradable, HCuSNPs are excreted from the liver and kidneys and are considered biodegradable [28, 34, 35]. Due to the extremely low solubility of CuS, CuS nanoparticles show much less toxicity than CuO nanoparticles [36].

Our aim was to investigate HCuSNPs-loaded microspheres, which combine photothermal, chemo- and radio-therapies with photoacoustic imaging and single photon emission computed tomography/computed tomography (SPECT/CT) imaging, delivered by arterial embolization in a single setting (Figure 1A) to Walker-256 tumor transplanted in rat liver. We incorporated HCuSNPs, as photothermal coupling agents, into poly (lactic-co-glycolic acid) (PLGA) microspheres to produce HCuSNPs-loaded microsphere (HCuSNPs-MS). The HCuSNPs-MS was labeled with iodine-131 (^{131}I) for SPECT/CT imaging and radiotherapy. Paclitaxel (PTX) was loaded into the microspheres for chemotherapy. We hypothesized that PTX-loaded and ^{131}I-labeled HCuSNPs-MS (^{131}I-HCuSNPs-MS-PTX) would have a combined therapeutic effect on the hepatic tumors (Figure 1B) and allow for SPECT/photoacoustic imaging to monitor the delivery of the microspheres *in vivo*.

Materials and Methods

Chemicals

Sodium sulfide (Na_2S), copper chloride ($CuCl_2$) and sodium perchlorate ($NaClO_4$) were supplied by Sigma-Aldrich (Saint Louis, MO, U.S.A.). Polyvinyl alcohol (PVA; MW ~74885, 88% hydrolyzed) was purchased from Aladdin (Shanghai, China). PLGA (lactide: glycolide = 50:50, viscosity = 0.55-0.75 dL/g) was purchased from Durect (Cupertino, USA). PTX was provided by Melone Pharmaceutic (Dalian, China). Na^{131}I was obtained from XinKe Corporation (Shanghai, China). Deionized water was obtained from a Milli-Q synthesis system (Millipore, Billerica, MA).

Preparation and characteristics of HCuSNPs-MS-PTX

HCuSNPs were synthesized according to the previously reported procedures [37]. PLGA microspheres (40 μm) containing PTX and HCuSNPs were prepared as follows: Briefly, an aqueous solution (0.2 mL) containing 3.2 mg of HCuSNPs was mixed with dichloromethane (2 mL) containing 50 mg of PLGA and 2.5 mg of PTX by the ultrasonic probe

(Scientz, China) to form the first emulsion. Then the emulsions were added to 2% polyvinyl alcohol (PVA) solution serving as the external aqueous phase, and homogenized to form a $w_1/o/w_2$ multiple emulsion. The emulsion was then poured into 0.5% PVA solution and stirred at 1000 rpm for 3 h using magnetic stirrer to evaporate the dichloromethane completely. Finally, the microspheres were separated by centrifugation at 3214 g for 10 min and the precipitate was washed three times with deionized water.

The morphology of the HCuSNPs and microspheres were measured by transmission electron microscopy (TEM, VEGA TS5136MM, TESCAN s.r.o., Brno, Czech Republic) and scanning electron microscopy (SEM, Tecnai G2 20 TWIN, FEI company, Hillsboro, USA). The size distributions of HCuSNPs and microspheres were measured by Zetasizer Nano-90 and Malvern Matersizer 3000 (Malvern, UK), respectively. The UV-visible spectra were measured by UV-2401PC UV/vis spectrophotometer (Shimadzu, Japan).

A 915-nm NIR laser light (MDL-III-915R, CNI, Changchun, China) was delivered through a quartz cuvette, containing HCuSNPs phosphate buffer saline (PBS) solution (1 mg/mL, 200 μL), HCuSNPs-MS PBS solution (23.98 mg/mL of MS containing 1 mg/mL of HCuSNPs, 200 μL) and PBS solution (200 μL) at an output power of 0.5 W/cm^2 over a period of 10 min to measure the photothermal effect of HCuSNPs-MS. The temperature was measured by a thermocouple, which was inserted into the solution during laser exposure. Long-term release of PTX from HCuSNPs-MS-PTX was investigated. The sample was prepared by suspending HCuSNPs-MS-PTX to form 0.55 mg/mL of MS (PTX, 25 μg/mL) solution with 0.5% Tween 80. Then MS solution (200 μL) was aspirated and added to an EP vial. The vials were kept in a 37 °C water bath. Three vials were centrifuged at 13523 g for 10 min at each time point. PTX concentration in the supernatant was measured by a high performance liquid chromatography (HPLC) system (LC-20AR, Shimadzu, Japan) with an SPD-M20AV photodiode array detector (Shimadzu, Japan). Additionally, NIR-light-triggered release of PTX from PLGA microspheres was performed. In brief, a HCuSNPs-MS-PTX precipitate (5.57 mg) or a MS-PTX precipitate suspended with PBS (0.01 M, 200 μL, pH 7.4) containing Tween 80 (0.5%, w/v) were aspirated into a quartz cuvette, respectively and irradiated using 915-nm NIR laser light (0.5 W/cm^2, 5 min) followed by 1.5 h intervals with the laser turned off and repeated three times. Before and after exposure each time, the solution was centrifuged at 3214 g for 5 min, and the supernatant was collected for free PTX determination. Then a fresh solution (200 μL) was added to suspend the precipitate for the next procedure. The HCuSNPs-MS-PTX solution without laser exposure was used as a control.

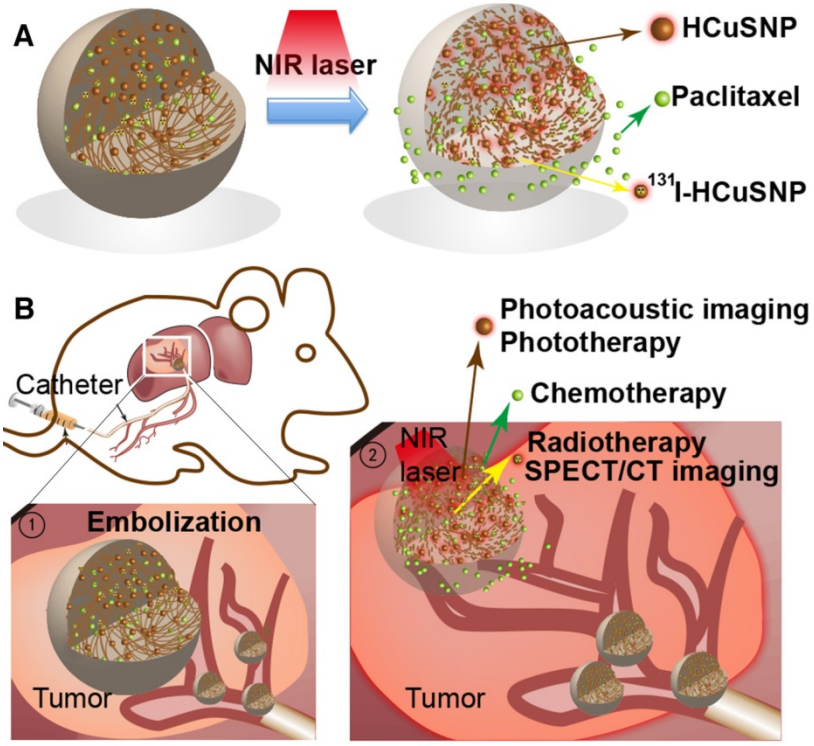

Figure 1. A, Schema shows structure of ^{131}I-HCuSNPs-MS-PTX. **B,** Outline of ^{131}I-HCuSNPs-MS-PTX for combined hepatic tumor arterial embolization in a rat liver tumor: Step 1, arterial embolization; Step 2, multimodal theranostics.

X-ray photoelectron spectroscopy (XPS) (PHI 5500, Perkin-Elmer, USA) was used to measure the surface elemental composition of the microsphere powders. The morphology of the cross-section of microspheres was observed by SEM. The loading efficiency of HCuSNPs in HCuSNPs-MS-PTX and HCuSNPs-MS was calculated by inductively coupled plasma optical emission spectrometry (ICP-OES) (ICAP6000, ThermoFisher Scientific, USA) analysis. For ICP-OES analysis, the microspheres solution was digested using a WX-6000 microwave system (PreeKem Corporation, Shanghai, China). In brief, ~10 μL of samples (50 mg/mL) were transferred into digestion vessels. After adding nitric acid (5 mL) to each vessel, the samples were digested for 20 min at 200 °C. Afterwards, the digested solution was evaporated to nearly dry and diluted with deionized water to a 10 mL of final volume for ICP-OES analysis.

Radiolabeling with ^{131}I

HCuSNPs-MS-PTX solution (0.2 mL, 12.5 mg) containing 0.72 ×10^{11} of HCuSNPs was mixed well with $Na^{131}I$ solution (0.2 mL, 37 MBq) and sodium perchlorate solution ($NaClO_4$) (0.8 mL, 0.1 mM), and then the mixture was incubated for 40 min at 32 °C. After adding deionized water (0.8 mL), the mixture was centrifuged at 67 g for 8 minutes at room temperature to rinse free $Na^{131}I$. The precipitate was suspended in normal saline solution (80 μL) to yield the final product. The radiolabeling yield was measured by thin-layer chromatography (TLC) using Whatman No.1 filter paper and deionized water was used as a developing solvent. The labeled microspheres remained at the original spot, while free ^{131}I ions shifted to the strip front. Then the filter paper was cut into two sections and each section was measured for radioactivity using a gamma counter (SN-697, Shanghai Institute of Nuclear Research, Rihuan Instrument Factory, Shanghai, China). The result was expressed as percentage of radioactivity of ^{131}I-HCuSNPs-MS-PTX relative to all radioactivity. The stability of radiolabeled ^{131}I-HCuSNPs-MS-PTX in serum was analyzed by incubating ^{131}I-HCuSNPs-MS-PTX in fetal bovine serum (FBS) (1:1, v/v) at 37 °C. The radiolabeling yield was measured by TLC at 1 h, 2 h, 4 h, 6 h, 12 h, 24 h, 48 h and 72 h, respectively.

Animal preparation

All the experiments were approved by Ren Ji Institutional Animal Care. Male Sprague Dawley rats (200-250 g) were purchased from Ren Ji Hospital Experimental Animal Center (Shanghai, China). Rats were kept under a specific pathogen-free condition at the laboratory animal center. To evaluate the biodistribution and therapeutic efficacy of ^{131}I-HCuSNPs-MS-PTX, we established Walker-256 tumor transplanted in rat liver [38]. Tumor transplantation was performed as follows: Walker-256 cells (5 × 10^6, 150 μL) were firstly injected subcutaneously in a donor rat. When the tumor diameter reached 6-8 mm, it was explanted from the donor rat and minced into small cubes of about 1 mm^3. The solid tumor fragment was inserted into the right liver lobe of the recipient rats. Ten days later, we performed ^{18}F-FDG micro-PET/CT scans to investigate the size of the liver tumor and when the diameter of liver tumor reached 6-8 mm, it was ready for the experiment.

Arterial Cannulation

Figure 2 represents the process of transcatheter arterial administration of ^{131}I-HCuSNPs-MS-PTX under a surgical microscope (Leica Microsystems, Weitzlar, Germany) according to a published method [38]. The celiac, hepatic and gastroduodenal arteries were identified and carefully dissected. Then two ligatures were placed around gastroduodenal artery and the distal part of the gastroduodenal artery was ligatured. A ligature was placed around the celiac artery to temporarily interrupt arterial flow. The gastroduodenal artery was punctured upstream of the distal ligature using a self-made needle and then a catheter was placed into the hepatic artery. After the administration of the microspheres, the proximal part of the gastroduodenal artery (upstream of the puncture point) was tied off. The ligature around the celiac artery was removed and hepatic arterial flow was restored.

Biodistribution and CuS staining

Three rats with transplanted tumors were given IA injection with ^{131}I-HCuSNPs-MS-PTX (80 μL, 10 mg, containing 0.5 mg of PTX, 0.58 ×10^{11} of HCuSNPs and 28 MBq of ^{131}I) to determine the distribution of the compound. Four hours post-administration, the rats were euthanized by inhalation of carbon dioxide. Blood, thyroid, lung, heart, spleen, stomach, intestine, colon, kidney, bladder, brain, bone, liver and the tumor were excised, weighed, and their radioactivity were measured by a gamma counter (SN-697, Shanghai Institute of nuclear research, Rihuan Instrument Factory, Shanghai, China). The organ uptake of ^{131}I-HCuSNPs-MS-PTX was calculated as %ID/g. To validate the copper distribution in the liver tumor, another 6 rats with transplanted tumors were randomly assigned to 2 groups (n = 3 in each group). All had IA injection with HCuSNPs-MS-PTX (80 μL, 10 mg, containing 0.5 mg of PTX and 0.58 ×10^{11} of HCuSNPs). One group was euthanized at 1 h

post-injection and the second group was euthanized at 4 h post-injection. The tumors were snap-frozen and then sectioned into contiguous 5-μm slices. A 5.0% silver nitrate aqueous solution (solution A) was used for CuS staining. An aqueous solution containing 2% hydroquinone and 5% citric acid was prepared as solution B. The slices were deparaffinized with xylene and graded alcohols and then exposed to freshly filtered solution that comprised 1 part solution A and 5 parts solution B for 3 min. The slices were then deionized with a water wash and then counterstained with hematoxylin.

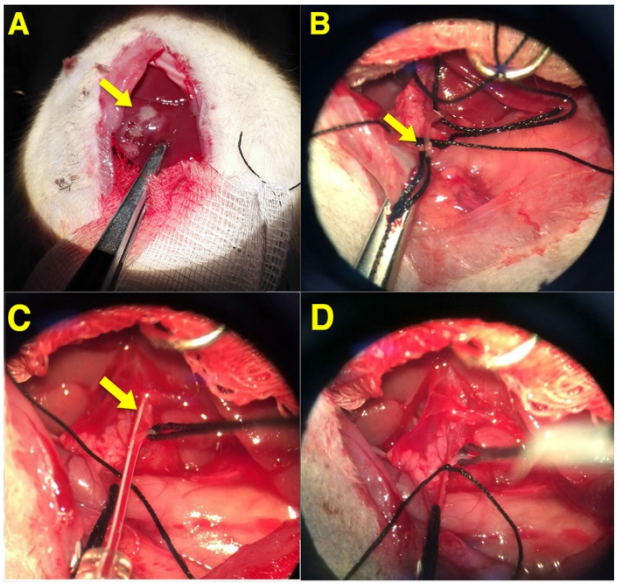

Figure 2. Intra-arterial injection of ^{131}I-HCuSNPs-MS-PTX via hepatic artery in rats bearing Walker-256 tumor transplanted in the liver. Tumor was observed under a surgical microscope (magnification 16 x). **A,** Liver tumor (yellow arrow). **B,** Coeliac, hepatic and gastroduodenal arteries were identified and the gastroduodenal artery (yellow arrow) was ligated with two sutures; the thread interrupts coeliac arterial flow temporarily. **C,** The gastroduodenal artery was punctured 'upstream' and a cannula was placed into the hepatic artery (yellow arrow). **D,** After the administration of the microspheres, the proximal gastroduodenal artery was tied off and the thread around the coeliac artery was removed.

Evaluation of the additional anticancer effect of the microspheres

The rats with transplanted tumors were randomly assigned to 6 groups (n = 5 in each). All rats received IA injections. The 6 groups (A-F) were as follows. Group A rats were injected with saline (control group, 80 μL). Group B rats were injected with ^{131}I-HCuSNPs-MS-PTX following laser irradiation (80 μL, 10 mg, containing 0.5 mg of PTX, 0.58 × 10^{11} of HCuSNPs and 28 MBq of ^{131}I). Group C rats were injected with ^{131}I-HCuSNPs-MS-PTX (80 μL, 10 mg, containing 0.5 mg of PTX, 0.58 × 10^{11} of HCuSNPs and 28 MBq of ^{131}I). Group D rats were injected with HCuSNPs-MS-PTX following laser irradiation (80 μL, 10 mg, containing 0.5 mg of PTX and 0.58 × 10^{11} of HCuSNPs). Group E rats were injected with ^{131}I-HCuSNPs-MS (80 μL, 10 mg, containing 0.58 × 10^{11} of HCuSNPs and 28 MBq of ^{131}I) following laser irradiation. Group F rats were injected with ^{131}I-HCuSNPs-MS (80 μL, 10 mg, containing 0.58 × 10^{11} of HCuSNPs and 28 MBq of ^{131}I). The NIR laser light had an output power of 0.5 W/cm^2 over a 5 min period. Laser irradiation was conducted at 4 h post-injection under the guide of photoacoustic imaging. We used an infrared thermal imaging camera (DT-980, CEM, Shanghai, China) during laser exposure to measure the tumor temperature over 6 min in each group.

^{18}F-FDG micro-PET/CT imaging

We used a micro-PET/CT scanner (Super Nova® PET/CT, PINGSENG Healthcare Inc., Shanghai, China) to measure ^{18}F-FDG uptakes in the rats. PET/CT scans were acquired at baseline prior to treatment and 1 d, 2 d, 4 d and 7 d post-injection of saline or microspheres. The spatial resolution of the PET/CT scanner is ~0.6 mm and the resolution of the CT is 0.2 mm. ^{18}F-FDG (0.3 mL, 37 MBq) was injected into the tail vein; the uptake period was 60 min and scan duration was 30 min. Rats were maintained under anesthesia with 2% isoflurane during scan acquisition. PET images were reconstructed with the ordered-subsets expectation maximization (OSEM) algorithm using 16 subsets and 4 iterations. An irregular region of interest, which covered the entire tumor, was drawn on the CT and then copied to the co-registered PET using Avatar 1.2 software (Pingseng, Shanghai, China). We measured the maximum transaxial diameters (length, width) of the tumors and the maximum standard uptake value (SUV_{max}). Tumor volumes were calculated as 0.5 × length × width^2 (mm^3) [39].

Histopathology and immunohistochemical staining

The animals were euthanized after ^{18}F-FDG micro-PET/CT scan on day 7. The tumors were harvested, snap-frozen with optimum cutting temperature compound (O.C.T., Sakura, San Francisco, USA) and then sectioned into 6 contiguous 5-μm slices. Two slices were stained with hematoxylin & eosin (H&E). Four slices were stored at -80 °C for immunohistochemical staining. Two slides were stained with terminal dexynucleotidyl transferase (TdT)-mediated dUTP nick end labeling (TUNEL) (Yeasen, Shanghai, China) according to the manufacturer's protocol. TUNEL-stained slides were analyzed under a fluorescence microscope (Zeiss Axio Observer.Z1, Oberkochen, CARL ZEISS, Germany).

Two slides were stained with anti-active Ki-67 polyclonal antibody according to the manufacturer's protocol (Novus, Colorado, USA). In addition, major organs (liver, kidney, spleen and lung) of rats in each group were dissected, embedded in O.C.T., snap frozen, and sectioned in 5-μm thick slices. The slices were stained with H&E for histological analysis.

Photoacoustic imaging and SPECT/CT imaging

The rats treated with ^{131}I-HCuSNPs-MS-PTX (80 μL, 10 mg, containing 0.5 mg of PTX, 0.58 × 10^{11} of HCuSNPs and 28 MBq of ^{131}I) plus laser irradiation underwent SPECT/CT imaging at 1 h, 4 h, 24 h, 48 h and 72 h post-injection. All rats were given water containing 0.12% potassium iodide (0.1 g of KI was added to 100 mL of drinking water) from 3 d before SPECT/CT imaging to minimize thyroid uptake of free ^{131}I. The SPECT/CT scanner (Precedence 6, Philip Medical Systems, Netherlands) had a variable-angle dual-detector with high-resolution collimators and a multislice spiral CT. The SPECT acquisition (128 × 128 matrix, 30 frames) was performed using 6° angular steps in 25 s time frames. After reconstruction, SPECT images were corrected for attenuation and scatter. CT scans were performed using a multislice CT scanner (PHILIPS Precedence, Philip Medical Systems, Netherland, 120 kV, 240 mA, 1 mm per scan). Reconstruction of transaxial slices was performed using filtered back projection (Metz filter power, 3.00; full width at half maximum, 10 mm) with subsequent attenuation correction using the Chang method (attenuation coefficient 0.12). SPECT/CT images were fused using Syntegra software (Philip Medical Systems, Netherlands).

Another three Rats that were injected with ^{131}I-HCuSNPs-MS-PTX underwent photoacoustic imaging. The rats were maintained under anesthesia with 1% isoflurane. The photoacoustic scans were conducted at 1 h, 2 h, 3 h and 4 h post-injection using a Vevo 2100 ultrasound/photoacoustic (PA) scanner with a LZ400 PA probe (30 MHz linear acoustic array transducer; VisualSonics Inc., Toronto, Canada). The tumor was located by B-mode (ultrasonic scan) and PA-mode. Clear gel was centrifuged (to remove air bubbles) and used to provide PA coupling between the probe and tumor. PA-mode was conducted in nanostepper mode using several laser wavelengths: 750 nm, 810 nm, 850 nm, 855 nm, 895 nm and 915 nm. A spectroscopically-separated multiplexer was used for data analysis in Vevo LAB software. Multispectral photoacoustic imaging was also performed to obtain measurements of hemoglobin. All imaging datasets were analyzed using the Vevo LAB (Ver 1.7.2) workstation software.

Statistical analysis

Group variation was described as the mean ± standard deviation (SD). The difference in tumor volume and SUV_{max} values on day 7 among multiple treatment groups was evaluated by one-way analysis of variance (ANOVA) followed by least-significant difference (LSD) post hoc multiple comparison tests (SPSS 22.0, USA). Differences between groups were considered statistically significant at $p < 0.05$, and $p < 0.001$ was considered highly statistically significant.

Results

Characterization of the synthesized microspheres

TEM images of HCuSNPs showed that the nanoparticles with hollow interior had a uniform size of 198.36 nm ± 4.85 nm in diameter (Figure 3A and B). The HCuSNPs had a peak absorbance intensity at 900 nm (Figure 3C). Following NIR light exposure (0.5 W/cm^2, 10 min), the temperature of PBS containing HCuSNPs-MS increased from 25.6 °C to 57.7 °C (ΔT = 32.1 °C) owing to the strong photothermal conversion effect of HCuSNPs incorporated in the microspheres (Figure 3D). In comparison, the temperature of PBS following laser irradiation did not obviously change.

The microspheres had an average size of 47.27 μm ± 0.5 μm (Figure 3E and F). The size of the microspheres can be controlled by stirring speed. The microspheres with mean sizes of 24.3 μm, 47.2 μm, and 76.6 μm were acquired under stirring at 1500 rpm, 1000 rpm and 500 rpm by magnetic stirrer, respectively. The loading content of HCuSNPs and loading efficiency of PTX in HCuSNPs-MS-PTX and HCuSNPs-MS are presented in Table 1. PTX was readily loaded into PLGA microspheres with > 95% encapsulation efficiency (Table 1). PTX release profile revealed a sustained and slow release of PTX from the PLGA microspheres with a cumulative release of 4.23% ± 0.92% at day 1 and 41.77% ± 3.78 % at day 7, without significant burst release (Figure 3G). A rapid release of PTX from HCuSNPs-MS-PTX was achieved when triggered by NIR light (Figure 3H). The light (0.5 W/cm^2, 915 nm) triggered ~3-4-fold of PTX release from HCuSNPs-MS-PTX within 5 min compared to the PTX release from the same microspheres for the initial 1.5 h but without laser irradiation. No rapid increase of PTX release was observed when PTX-MS was exposed to the laser, indicating that the photothermal effect mediated by HCuSNPs accelerated the release of PTX.

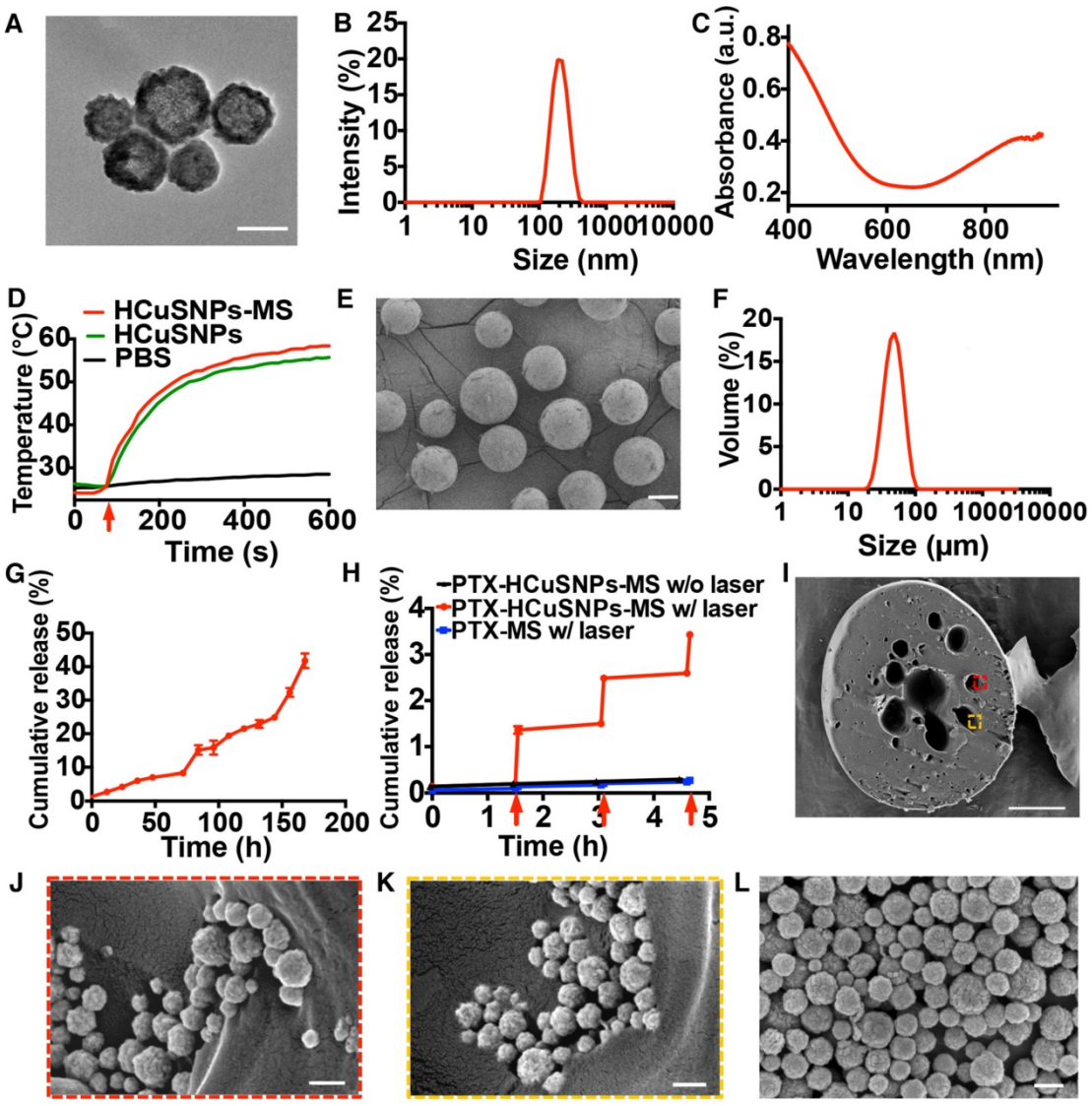

Figure 3. A, Transmission electron microscopy images of HCuSNPs. Bar, 100 nm. **B,** Size distribution of HCuSNPs. **C,** Absorbance spectrum of HCuSNPs in water. **D,** Temperature-time profiles of HCuSNPs-MS in PBS (200 μL, 23.98 mg/mL of MS containing 1 mg/mL of HCuSNPs), HCuSNPs in PBS (200 μL, 1 mg/mL) and PBS (200 μL) under NIR laser irradiation (915 nm, 0.5 W/cm^2, 10 min). Red arrow indicates laser switched on. **E,** Scanning electron microscopy images of HCuSNPs-MS-PTX. Bar, 20 μm. **F,** Size distribution of HCuSNPs-MS-PTX. **G,** Cumulative release of PTX from HCuSNPs-MS-PTX. **H,** NIR light-triggered release of PTX from HCuSNPs-MS-PTX. NIR laser light (915 nm, 0.5 W/cm^2, 5 min). Red arrows indicate laser switched on. **I,** Scanning electron micrographs of the cross-section of HCuSNP-MS-PTX. Bar, 10 μm. **J, K,** Enlarged area in (I). **L,** SEM image of HCuSNPs. Bars in (J), (K) and (I), 200 nm.

Table 1. Characteristics of the microspheres.

Microspheres	HCuSNPs loading (w/w,%)	Encapsulation efficiency of PTX loading (%)
HCuSNPs-MS-PTX	3.18 ± 0.27	96.75 ± 0.42
MS-PTX	----	99.36 ± 0.03
HCuSNPs-MS	4.17 ± 0.10	----

The XPS lineshapes reveal that the two peaks located at 932.2 eV and 952.2 eV are assigned to Cu 2p3/2 and Cu 2p1/2 of HCuSNP, respectively. The peak at 162 eV corresponds to S 2p of HCuSNP. By contrast, there were no peaks detected in MS and MS-PTX powders without HCuSNP-loading (Figure S1). The SEM images showed many pores spreading over the cross-section of the microspheres, which were probably formed during the drying process of the internal water phase (Figure 3I). It was obvious that the HCuSNPs existed in the pores (Figure 3J, K and L). These SEM images evidenced that HCuSNPs were successfully loaded into the microspheres.

In the previous report [40], copper (I) sulfide could absorb iodide by replacing hydroxyl groups on the surface (Equation 1), similar to what was observed for adsorption of iodide on Cu_2O in neutral or alkaline medium. The Cu/S compositional ratio (63.49%: 36.51%) of HCuSNPs detected by scanning electron microscopy-energy dispersive spectrometry (SEM-EDS) indicated that there was copper (I) sulfide in HCuSNPs. ^{131}I thus can be labeled on the HCuSNPs

through formation of copper (I)-iodide complexes. The radiolabeling yield and specific activity of ^{131}I-HCuSNPs-MS-PTX were ~97% and ~2.9 MBq/mg, respectively. The final radioactivity concentration of ^{131}I-HCuSNPs-MS-PTX was ~0.45 MBq/μL. Finally, we measured ^{131}I-HCuSNPs-MS-PTX (12.5 mg, 80 μL) containing 0.63 mg of PTX, 0.73 × 10^{11} of HCuSNPs and 35 MBq of ^{131}I. The radiolabeling yield remained at 97% in saline after 24 h, whereas, the radiolabeling yield of ^{131}I-HCuSNPs-MS-PTX in serum remained at ~70.2% at 48 h.

Equation 1. The mechanism for ^{131}I labeling of the HCuSNPs:

$$\equiv Cu{-}OH + I^- \longrightarrow \equiv Cu{-}I + OH^-$$

Distribution of ^{131}I-HCuSNPs-MS-PTX following transcatheter arterial embolization

Biodistribution results showed that at 4 h post-injection, the tumor uptake of ^{131}I-HCuSNPs-MS-PTX was as high as 3.15 %ID/g ± 0.49 %ID/g (Figure 4A). IA injection of ^{131}I-HCuSNPs-MS-PTX resulted in higher nanoparticle accumulation in the tumor than in normal liver tissues (tumor-to-liver ratio 1.41 ± 0.14). Remarkably, lung uptake of ^{131}I-HCuSNPs-MS-PTX was only 0.30 %ID/g ± 0.05 %ID/g. Tumor-to-lung ratio of ^{131}I-HCuSNPs-MS-PTX was 7.58 ± 1.76 and the rats did not display tachypnea, cyanosis, tachycardia or acute death after injection, indicating that the IA injection did not produce pulmonary embolism. Moreover, ^{131}I-HCuSNPs-MS-PTX showed lower retention in the stomach, spleen and thyroid gland. To confirm the embolization effect of the HCuSNPs-MS-PTX, we stained the CuS of the microspheres in the rat liver sections with the transplanted tumors following IA administration. Figure 4B shows that the IA-administered HCuSNPs-MS-PTX filled the blood vessels in tumor marginal zones in clusters at 1 h or 4 h following injection. At 4 h post-injection there was tumor necrosis in the region of tumor surrounding the microspheres (Figure 4B). The histological results indicated that HCuSNPs-MS-PTX efficiently embolized transplanted liver tumor causing tumor necrosis at 4 h post-injection.

Combinatorial anticancer effect of ^{131}I-HCuSNPs-MS-PTX

Infrared thermal imaging of the treated tumor-bearing rats showed tumor temperature quickly elevated from 35.2 °C to 43 °C within 1 min upon NIR laser exposure (0.5 W/cm^2, 915 nm) then gradually reaching a plateau of ~45 °C (Figure 5). In contrast, the tumor-bearing rats treated with ^{131}I-HCuSNPs-MS-PTX but without laser exposure did not show any change of temperature.

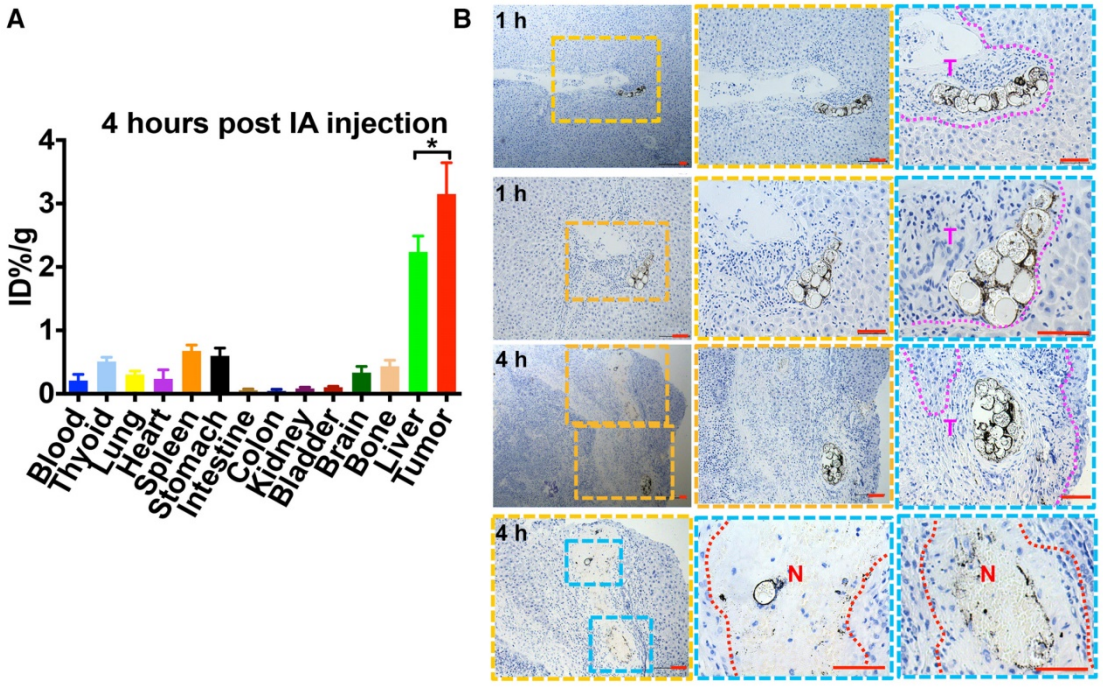

Figure 4. A, Biodistribution of ^{131}I-HCuSNPs-MS-PTX at 4 h post intra-arterial (IA) injection. *p < 0.05, significant difference in values between the two groups. Data are presented as mean ± SD. n = 3. **B,** CuS staining of Walker-256 tumor transplanted in rat liver at 1 h and 4 h post IA injection. Purple dotted lines, HCuSNPs-MS-PTX in capillaries of tumor marginal zones. Red dotted lines, HCuSNPs-MS-PTX in tumor necrotic area with marked loss of tumor cell nuclei. T, tumor. N, necrotic region. Bar, 50 μm.

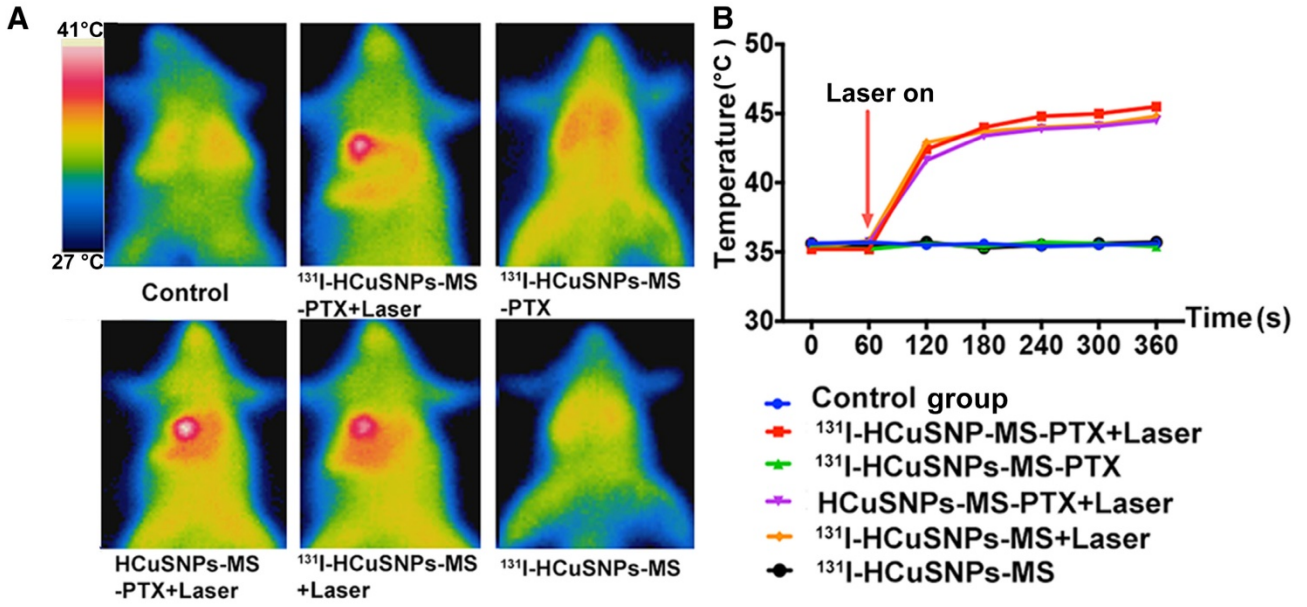

Figure 5. A, Thermal imaging of tumor-bearing rats after IA injection with different formulations with or without laser treatment (915 nm, 0.5 W/cm², 5 min). **B,** Temperature-time profile of tumors following different treatments.

Figure 6A illustrates the experimental design to evaluate the combinatorial therapeutic effect of ^{131}I-HCuSNPs-MS-PTX in rats bearing Walker-256 tumor transplanted in liver. We used ^{18}F-FDG micro-PET/CT imaging to monitor the tumor response following different treatments. Representative ^{18}F-FDG micro-PET/CT images showed that tumoral ^{18}F-FDG uptake increased in the control group that was not treated (Figure 6B). ^{131}I-HCuSNPs-MS-PTX plus laser treatment produced a significant (p = 0.016, p < 0.05) reduction in ^{18}F-FDG uptake in the tumor at 1 d post-treatment. There was no ^{18}F-FDG uptake at 7 d post-treatment, consistent with an absence of viable tumor. In comparison, tumor-bearing rats that were treated with HCuSNPs-MS-PTX plus laser irradiation showed decreased tumoral ^{18}F-FDG uptake at 1 d post-treatment but ^{18}F-FDG uptake quickly increased at the tumor marginal site after 2 days, consistent with tumor recurrence. ^{131}I-HCuSNPs-MS-PTX and ^{131}I-HCuSNPs-MS only slowed the tumor growth, when compared to the control rats, but were unable to stop tumor growth.

We quantified tumor volume using micro-CT. In the control group, there was a marked increase in tumor volume from 85.04 mm^3 ± 15.46 mm^3 (day 0) to 1015.31 mm^3 ± 89.59 mm^3 (day 7; Figure 6C); SUV_{max} of tumor increased from 5.61 ± 0.39 to 8.88 ± 0.30 during 7 d post-treatment (Figure 6D). In contrast, there was minimal change in tumor volume in the rats treated with ^{131}I-HCuSNPs-MS-PTX and concomitant laser exposure between day 0 and day 7 (86.54 mm^3 ± 22.35 mm^3 vs. 88.63 mm^3 ± 11.66 mm^3, p = 0.86; Figure 6C); SUV_{max} in the same cohort, however, reduced to 1.03 ± 0.18, similar to background, at day 7 post-treatment (Figure 6D), suggesting that the tumors were not viable. In comparison, embolization in combination with one or two therapy modalities slowed but did not stop tumor growth; SUV_{max} decreased within 1 d but quickly recovered at 2 d post-injection and further increased after treatment.

Figure 7A shows photographs of all the liver tumors at day 7 after different treatments. Consistent with the results of ^{18}F-FDG PET/CT imaging, we found that the tumor size of rats treated with ^{131}I-HCuSNPs-MS-PTX plus laser were the smallest. The results of H&E staining, TUNEL and Ki-67 staining confirmed our ^{18}F-FDG micro-PET/CT results (Figure 7B). Tumor cells in the control group displayed heteromorphism and heteropyknosis with notable increases in nucleus/plasma ratios, high expression of Ki-67 and little apoptosis (Figure 7B). In the rats treated with ^{131}I-HCuSNPs-MS-PTX plus laser, tumor cells displayed characteristics of necrosis with complete nuclear loss, little to no expression of Ki-67 and marked apoptosis (Figure 7B). In other treatment groups, necrosis was localized mostly in the center of tumors and Ki-67 was mainly localized to the tumor periphery where there were only a few TUNEL positive cells (Figure 7B). These results further demonstrated that ^{131}I-HCuSNPs-MS-PTX plus laser exposure induced marked tumor apoptosis and almost complete inhibition of proliferation.

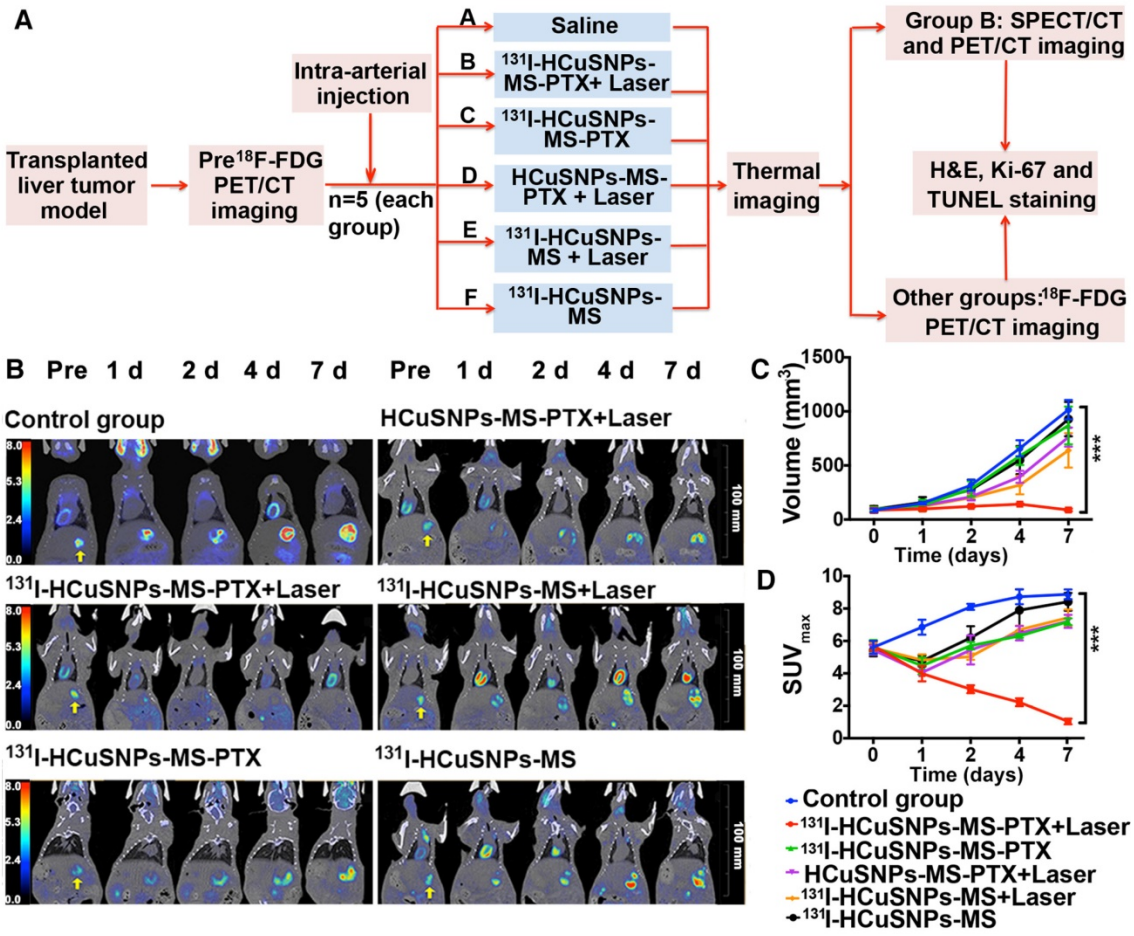

Figure 6. A, Experimental design of our combined theranostic approach. **B,** Representative ^{18}F-FDG micro-PET/CT images. Arrows indicate tumors. **C,** Tumor volumes of different groups at different time-points. **D,** Tumor SUV_{max} of different groups at different time-points. SUV_{max}, maximum standard uptake value. ***$p < 0.001$, significant difference in values between the two groups on day 7. Data are presented as mean ± SD. n = 5.

H&E staining (Figure S2) of the major organs (liver, kidney, spleen and lung) did not show any obvious histopathological abnormalities (i.e., tissue damage, inflammation or lesions). Further work is needed to systematically study the potential short- and long-term toxicity of ^{131}I-HCuSNPs-MS-PTX after the IA injections. Furthermore, ^{131}I-HCuSNPs-MS-PTX accumulated in tumor blood vessels and occluded them 7 d after IA injection (Figure 8). Rats treated with ^{131}I-HCuSNPs-MS-PTX plus laser showed nearly complete tumor necrosis without discernable tumor blood vessels and the microspheres were seen in the necrotic tissue but without microspheres in the normal liver tissue (Figure 8).

SPECT/CT and photoacoustic imaging

SPECT/CT imaging provided the whole-body distribution of ^{131}I-HCuSNPs-MS-PTX post IA injection of ^{131}I-HCuSNPs-MS-PTX (Figure 9A). ^{131}I-HCuSNPs-MS-PTX was mainly found in the liver tumor and there was minimal uptake in the rest of the organs, in particular the lungs. Moreover, the SPECT/CT scanning confirmed that the ^{131}I stayed in tumors for 48 h following the IA administration (Figure 9A). From the photoacoustic images, the microsphere distribution in the tumor had photoacoustic signal intensities of 0.058 a.u., 0.048 a.u., 0.064 a.u. and 0.077 a.u. at 1 h, 2 h, 3 h and 4 h post-injection, respectively (Figure 9B).

Discussion

In this work we developed a multifunctional agent that provides TACE and ablation sequentially. The present study's findings validated the characteristics of the multifunctional microspheres. The PLGA microspheres had high encapsulating efficiency of the lipophilic drug PTX, accompanied by uniform particle size and a steady drug release rate [41]. The incorporated HCuSNPs exhibited a reliable photothermal coupling effect independent of the microsphere encapsulation, which ensured the efficacy of molecular imaging, photothermal therapy, drug delivery, and cancer treatment [28, 30, 42]. The process of labeling nanoparticles with ^{131}I was simple and straightforward, providing feasibility of radiotherapy and SPECT/CT imaging [43, 44].

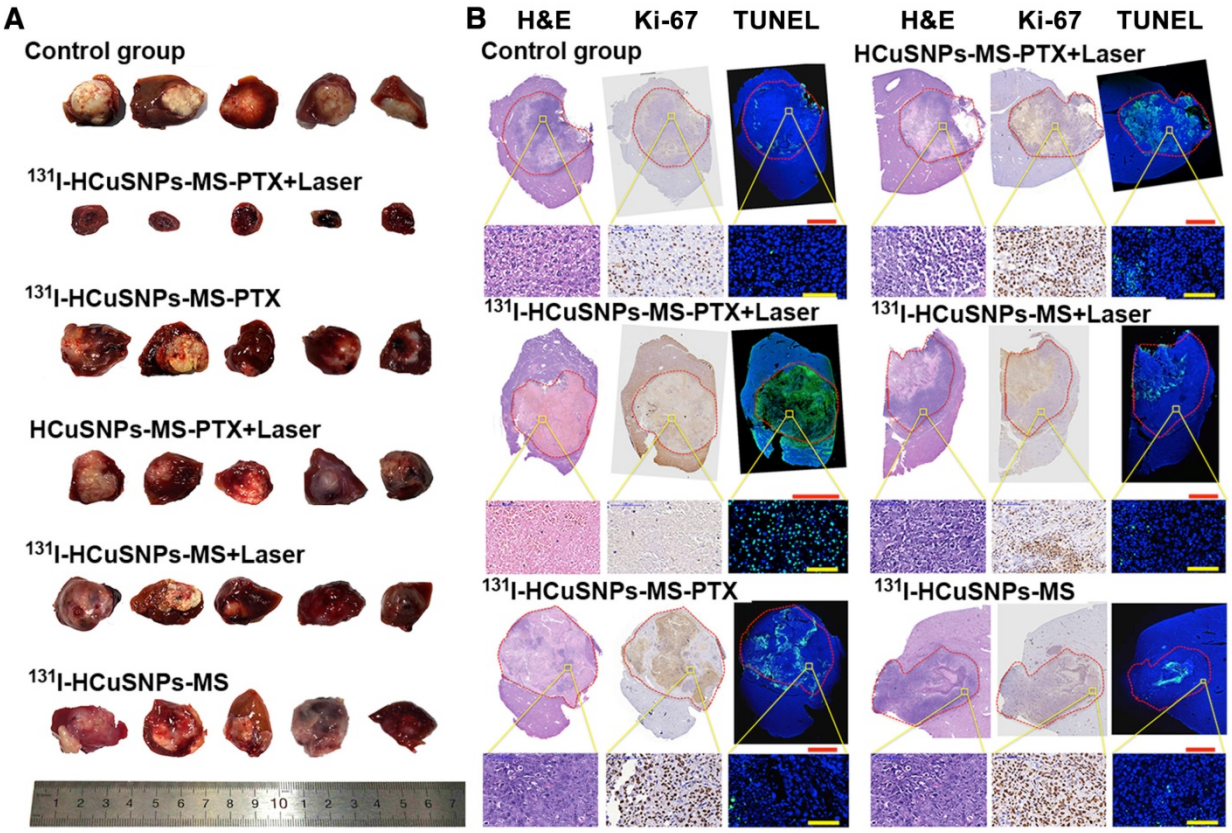

Figure 7. A, Photograph of all the liver tumors at day 7 after different treatments. **B,** H&E, Ki-67 and TUNEL staining following different treatments. Laser, 915 nm, 0.5 W/cm^2, 5 min. Green, TUNEL-positive apoptotic cells. Blue, 4',6-diamidino-2-phenylindole (DAPI)-stained nuclei. Red circle regions, tumors. Bar in red, 5 mm. Bar in yellow, 100 μm.

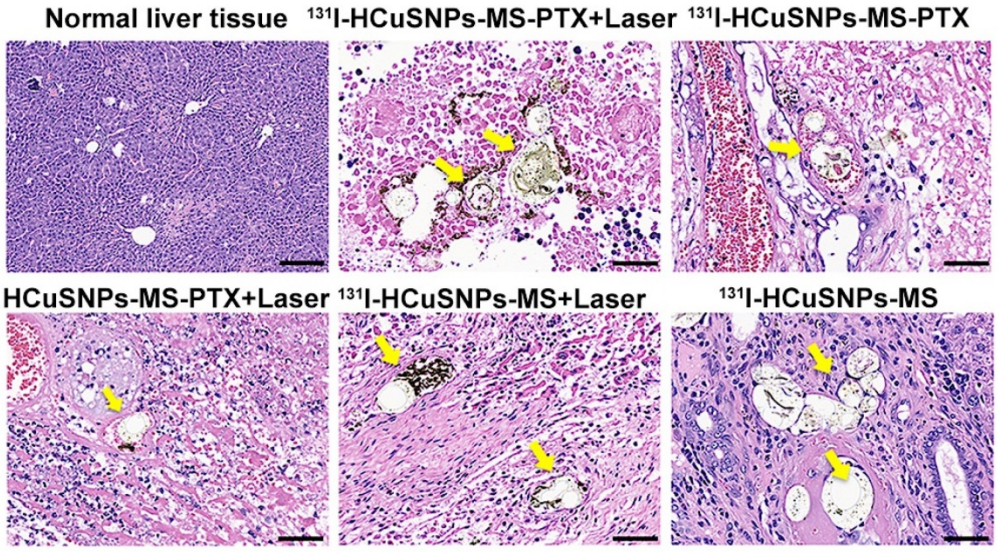

Figure 8. H&E sections from tumor bearing rats treated with microspheres on day 7 showing the normal liver (top left image) and liver tumors (the rest of the images). Microspheres were seen in tumor blood vessels and were surrounded by necrotic tissue; microsphere were not seen in normal liver. Yellow arrows, microspheres. Bar, 50 μm.

PTX is widely used to treat a variety of cancers [45]. Walker-256 tumor (breast cancer) model is rather sensitive to PTX [46], so we loaded PTX into the microspheres. The laser-triggered release of PTX synergized the antitumor effect of PTT since hyperthermia potentiated the tumor cell killing effect of PTX [47]. Any residual tumor cells remaining after laser treatment were eradicated through a combined effect of the sustained-released PTX, and the ^{131}I-beta rays, which have a tissue penetration of ~2 mm [48]. According to our results reported here, tumor can be eradicated completely due to the synergistic effect of

the above three treatment modalities.

Our results show that complete inhibition of Walker-256 tumor growth in rat liver via IA injection of ^{131}I-HCuSNPs-MS-PTX can be achieved at a low dose due to the synergistic effects of embolization, chemotherapy, PTT, and ^{131}I radiation therapy. Embolization of microspheres produced vascular occlusion resulting in nutritional tumor deprivation [49]. An early study revealed that microparticles less than 40 μm in diameter could distribute to non-targeted organs, such as the lungs, while microparticles larger than 40 μm in diameter were mainly trapped in the liver tumor tissue and rarely washed out into other organs [50]. In our study, the lung distribution of ^{131}I-HCuSNPs-MS-PTX was low and the microspheres did not produce pulmonary embolism because their average size was 47.27 μm in diameter, larger than 40 μm. Localized PTT induced tumor ablation; a sublethal dose of hyperthermia at the margins of the tumor resulted in tumor recurrence, as shown by the relatively high metabolism in these areas shown in Figure 6B. Incomplete ablation was mainly caused by the 'heat sink' effect due to the conductive effects of adjacent vessels [51]. IA embolization overcomes the heat sink effect and improves the effectiveness of TACE-RFA [52, 53]. In the clinic, however, the implementation of TACE-RFA is complex.

Although TACE has been the first-line treatment for patients with intermediate hepatocarcinoma cancer (HCC) for years, there is not a standard global approach to the way TACE is used. There are variations in technique and embolic and chemotherapeutic agents used, which all affect its efficacy [54, 55]. A 'best' chemotherapeutic/embolic agent is yet to be developed. In the clinic, cTACE, which typically comprises a mixture of the chemotherapeutic in lipiodol (ethiodized poppy seed oil), is used to occlude tumor blood vessels and release the chemotherapeutic agents. Lipiodol, however, may release the drug rapidly and have an incomplete embolic effect [56, 57]. When compared to the cTACE embolic agents, our agent ^{131}I-HCuSNPs-MS-PTX has several advantages: a) Drug release from the embolic microspheres can be controlled by the photothermal effect of the nanoparticles. Notably, the microsphere sustained release of the chemotherapeutic over time without laser exposure. b) The amount of chemotherapy agent loaded into the MS can be individually tailored, thus allowing for more 'precise' and 'personalized' treatment. c) The diameter of ^{131}I-HCuSNPs-MS-PTX is adjustable to achieve effective embolization. d). When compared to lipiodol, the size of our microspheres allows for easier injection during the procedure.

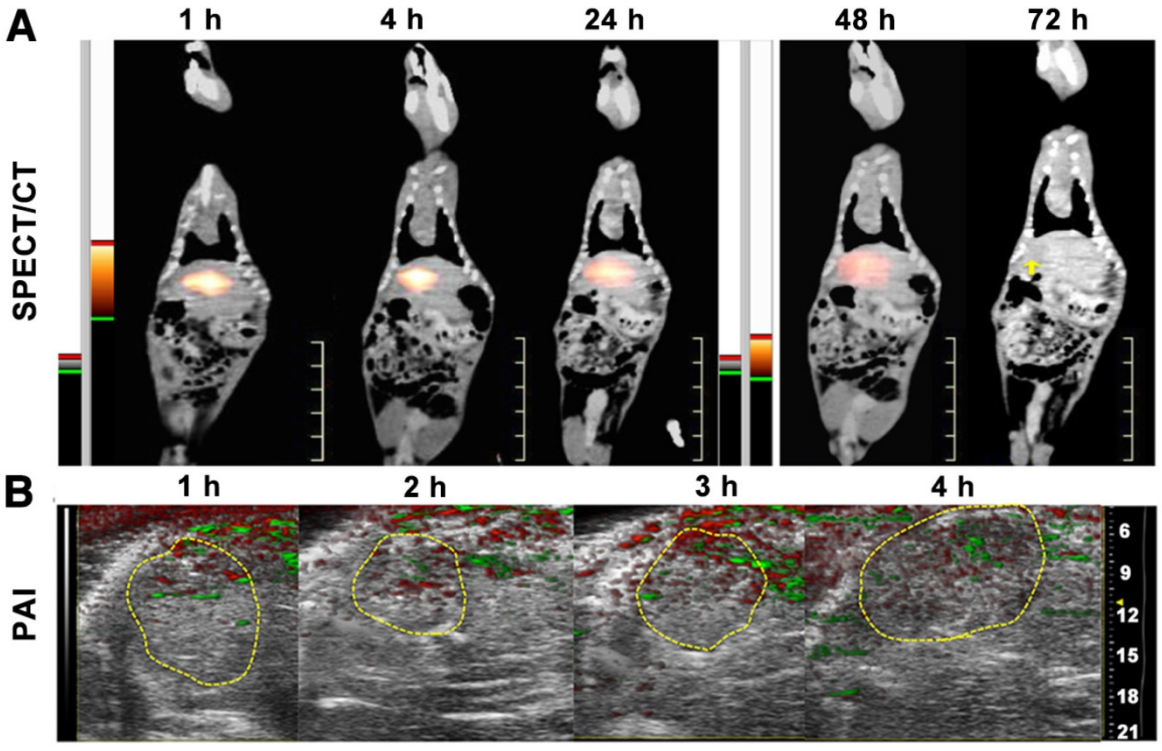

Figure 9. A, SPECT/CT scans of tumor-bearing rats after IA injection of ^{131}I-HCuSNPs-MS-PTX (80 μL, 10 mg, containing 0.5 mg of PTX, 0.58 × 10^{11} of HCuSNPs and 28 MBq of ^{131}I) showed that tracer uptake localized to the hepatic tumor (yellow arrow indicates site of tumor). **B,** Photoacoustic imaging (PAI) of liver in the tumor-bearing rats after IA injection of ^{131}I-HCuSNPs-MS-PTX (80 μL, 10 mg, containing 0.5 mg of PTX, 0.58 × 10^{11} of HCuSNPs and 28 MBq of ^{131}I). Green indicates photoacoustic signals of ^{131}I-HCuSNPs-MS-PTX; red reflects photoacoustic signal of hemoglobin.

Transcatheter arterial radiation embolization (TARE) uses microspheres containing Yttrium-90 (^{90}Y) to suppress tumor growth [58, 59], which is well tolerated and has a low complication rate due to the limited radiation range of beta rays. However, the main disadvantage of TARE is that ^{90}Y is unable to carry chemotherapeutic agents and the tolerable radiation dose of the liver tissue limits retreatment with TARE [60]. Although TACE provides a survival benefit in patients with intermediate HCC, it may result in suboptimal and incomplete tumor responses [13]. Further, repeat TACE has the risk of producing hepatic dysfunction and reducing patient survival. DEB-TACE was developed for transcatheter delivery to the liver tumor and it permits sustained drug release into the tumor vasculature [61, 62]. Nicolini *et al.* showed that complete necrosis was achieved in 77% of tumors in the DEB group and only 27% of tumors in the bland embolization group [63]. Nevertheless, there are instances where there is incomplete/ineffective treatment because insufficient quantities of the embolic/drug are delivered and tumor resistance to the drug [14]. In addition, some investigators suggest that residual tumor cells can transform into a more malignant phenotype when there is incomplete tumor cell death [64, 65]. It is accepted that tumor heterogeneity contributes to different responses to monotherapy, which has promoted the development of combined therapies with TACE [66].

Additionally, our work showed that SPECT/photoacoustic imaging mediated by ^{131}I-HCuSNPs-MS-PTX could help to confirm the delivery of the microspheres to the targeted tumors and to guide therapy planning for near-infrared laser irradiation. Previous studies have focused on embolic microsphere detection with CT and magnetic resonance (MR) imaging [67-69]; however, the high sensitivity of SPECT/CT and high specificity of photoacoustic imaging in our study obviated the need for additional imaging.

Conclusions

In this study, we synthesized and validated a combined therapeutic and imaging compound, ^{131}I-HCuSNPs-MS-PTX, for the treatment of the Walker-256 tumor transplanted into rat liver. IA injection of ^{131}I-HCuSNPs-MS-PTX embolized the tumor vascular supply and delivered chemo-, photo- and radio-therapy locally and ablated the transplanted tumor. In addition, SPECT/CT and photoacoustic imaging of the microspheres confirmed that the embolized compound reached the targeted sites. We suggest that our findings offer the potential for using IA administration of ^{131}I-HCuSNPs-MS-PTX in the clinic.

Abbreviations

PLGA: polylactic-co-glycolic acid; HCuSNPs: hollow copper sulfide nanoparticles; PTX: Paclitaxel; MS: microsphere; SPECT: single photon emission computed tomography; ^{18}F-FDG: ^{18}F-Fluorodeoxyglucose; PET/CT: positron emission tomography/computed tomography; RFA: radiofrequency ablation; TACE: transarterial chemoembolization; PEI: percutaneous ethanol injection; IA: intra-arterial; DEB: drug-eluting beads; NIR: near-infrared; PTT: photothermal therapy; PVA: polyvinyl alcohol; TEM: transmission electron microscopy; SEM: scanning electron microscopy; PBS: phosphate buffer saline; HPLC: high-performance liquid chromatography; XPS: X-ray photoelectron spectroscopy; ICP-OES: inductively coupled plasma optical emission spectrometry; TLC: thin-layer chromatography; FBS: fetal bovine serum; OSEM: ordered-subsets expectation maximization; SUVmax: maximum standard uptake value; O.C.T.: optimum cutting temperature; H&E: hematoxylin & eosin; TUNEL: terminal dexynucleotidyl transferase (TdT)-mediated dUTP nick end labeling; PA: photoacoustic; SD: standard deviation; ANOVA: analysis of variance; LSD: least-significant difference; SEM-EDS: scanning electron microscopy-energy dispersive spectrometry; HCC: hepatocarcinoma cancer; TARE: Transcatheter arterial radiation embolization; MR: magnetic resonance.

Acknowledgment

We thank Robert Rodgers from the University of Rhode Island for editing the manuscript. This work was partially supported by National Natural Science Foundation of China (81771861, 81471708, 81673018, 81530053, 81471685), the award of the "National Youth Thousand Talents Plan" of China, the Program for Professor of Special Appointment (Eastern Scholar) at Shanghai Institutions of Higher Learning (No.2012-05), Shanghai Municipal Education Commission—Gaofeng Clinical Medicine Grant Support (No.20172010), the program of Shanghai Municipal Commission of Health and Family Planning (201440606).

Supplementary Material

Supplementary figures.
http://www.thno.org/v08p0785s1.pdf

Competing Interests

The authors have declared that no competing interest exists.

References

1. Jemal A, Bray F, Center MM, Ferlay J, Ward E, Forman D. Global cancer statistics. CA Cancer J Clin. 2011; 61:69-90.
2. Abbruzzese JL, Abbruzzese MC, Lenzi R, Hess KR, Raber MN. Analysis of a diagnostic strategy for patients with suspected tumors of unknown origin. J Clin Oncol. 1995; 13:2094-103.
3. El-Serag HB. Hepatocellular carcinoma. N Engl J Med. 2011; 365:1118-27.
4. Bruix J, Sherman M, American Association for the Study of Liver D. Management of hepatocellular carcinoma: an update. Hepatology. 2011; 53:1020-2.
5. Donadon M, Solbiati L, Dawson L, Barry A, Sapisochin G, Greig PD, et al. Hepatocellular Carcinoma: The Role of Interventional Oncology. Liver Cancer. 2016; 6:34-43.
6. Sangiovanni A, Colombo M. Treatment of hepatocellular carcinoma: beyond international guidelines. Liver Int. 2016; 36 (Suppl):124-9.
7. Poon RT, Fan ST, Tsang FH, Wong J. Locoregional therapies for hepatocellular carcinoma: a critical review from the surgeon's perspective. Ann Surg. 2002; 235:466-86.
8. Peng ZW, Zhang YJ, Chen MS, Xu L, Liang HH, Lin XJ, et al. Radiofrequency ablation with or without transcatheter arterial chemoembolization in the treatment of hepatocellular carcinoma: a prospective randomized trial. J Clin Oncol. 2013; 31:426-32.
9. Peng ZW, Zhang YJ, Liang HH, Lin XJ, Guo RP, Chen MS. Recurrent hepatocellular carcinoma treated with sequential transcatheter arterial chemoembolization and RF ablation versus RF ablation alone: a prospective randomized trial. Radiology. 2012; 262:689-700.
10. Lewis AL, Gonzalez MV, Lloyd AW, Hall B, Tang Y, Willis SL, et al. DC bead: in vitro characterization of a drug-delivery device for transarterial chemoembolization. J Vasc Interv Radiol. 2006; 17:335-42.
11. Varela M, Real MI, Burrel M, Forner A, Sala M, Brunet M, et al. Chemoembolization of hepatocellular carcinoma with drug eluting beads: efficacy and doxorubicin pharmacokinetics. J Hepatol. 2007; 46:474-81.
12. Golfieri R, Giampalma E, Renzulli M, Cioni R, Bargellini I, Bartolozzi C, et al. Randomised controlled trial of doxorubicin-eluting beads vs conventional chemoembolisation for hepatocellular carcinoma. Br J Cancer. 2014; 111:255-64.
13. Song MJ, Chun HJ, Song DS, Kim HY, Yoo SH, Park CH, et al. Comparative study between doxorubicin-eluting beads and conventional transarterial chemoembolization for treatment of hepatocellular carcinoma. J Hepatol. 2012; 57:1244-50.
14. Lewis AL, Dreher MR. Locoregional drug delivery using image-guided intra-arterial drug eluting bead therapy. J Control Release. 2012; 161:338-50.
15. Li J, Zhou M, Liu F, Xiong C, Wang W, Cao Q, et al. Hepatocellular Carcinoma: Intra-arterial Delivery of Doxorubicin-loaded Hollow Gold Nanospheres for Photothermal Ablation-Chemoembolization Therapy in Rats. Radiology. 2016; 281:427-35.
16. Wen X, Reynolds L, Mulik RS, Kim SY, Van Treuren T, Nguyen LH, et al. Hepatic Arterial Infusion of Low-Density Lipoprotein Docosahexaenoic Acid Nanoparticles Selectively Disrupts Redox Balance in Hepatoma Cells and Reduces Growth of Orthotopic Liver Tumors in Rats. Gastroenterology. 2016; 150:488-98.
17. Her S, Jaffray DA, Allen C. Gold nanoparticles for applications in cancer radiotherapy: Mechanisms and recent advancements. Adv Drug Deliv Rev. 2017; 109:84-101.
18. Shanmugam V, Selvakumar S, Yeh CS. Near-infrared light-responsive nanomaterials in cancer therapeutics. Chem Soc Rev. 2014; 43:6254-87.
19. Zhou M, Song S, Zhao J, Tian M, Li C. Theranostic CuS Nanoparticles Targeting Folate Receptors for PET Image-Guided Photothermal Therapy. J Mater Chem B Mater Biol Med. 2015; 3:8939-48.
20. Liu D, Yang F, Xiong F, Gu N. The Smart Drug Delivery System and Its Clinical Potential. Theranostics. 2016; 6:1306-23.
21. Perez-Herrero E, Fernandez-Medarde A. Advanced targeted therapies in cancer: Drug nanocarriers, the future of chemotherapy. Eur J Pharm Biopharm. 2015; 93:52-79.
22. Miao Q, Lyu Y, Ding D, Pu K. Semiconducting Oligomer Nanoparticles as an Activatable Photoacoustic Probe with Amplified Brightness for In Vivo Imaging of pH. Adv Mater. 2016; 28:3662-8.
23. Zhang R, Pan D, Cai X, Yang X, Senpan A, Allen JS, et al. alphaVbeta3-targeted copper nanoparticles incorporating an Sn 2 lipase-labile fumagillin prodrug for photoacoustic neovascular imaging and treatment. Theranostics. 2015; 5:124-33.
24. Chen L, Zhong X, Yi X, Huang M, Ning P, Liu T, et al. Radionuclide (131)I labeled reduced graphene oxide for nuclear imaging guided combined radio- and photothermal therapy of cancer. Biomaterials. 2015; 66:21-8.
25. Lin LT, Chang CH, Yu HL, Liu RS, Wang HE, Chiu SJ, et al. Evaluation of the therapeutic and diagnostic effects of PEGylated liposome-embedded 188Re on human non-small cell lung cancer using an orthotopic small-animal model. J Nucl Med. 2014; 55:1864-70.
26. Pissuwan D, Nose K, Kurihara R, Kaneko K, Tahara Y, Kamiya N, et al. A solid-in-oil dispersion of gold nanorods can enhance transdermal protein delivery and skin vaccination. Small. 2011; 7:215-20.
27. Li Y, Lu W, Huang Q, Huang M, Li C, Chen W. Copper sulfide nanoparticles for photothermal ablation of tumor cells. Nanomedicine (Lond). 2010; 5:1161-71.
28. Ramadan S, Guo L, Li Y, Yan B, Lu W. Hollow copper sulfide nanoparticle-mediated transdermal drug delivery. Small. 2012; 8:3143-50.
29. Ku G, Zhou M, Song S, Huang Q, Hazle J, Li C. Copper sulfide nanoparticles as a new class of photoacoustic contrast agent for deep tissue imaging at 1064 nm. ACS Nano. 2012; 6:7489-96.
30. Zhou M, Ku G, Pageon L, Li C. Theranostic probe for simultaneous in vivo photoacoustic imaging and confined photothermolysis by pulsed laser at 1064 nm in 4T1 breast cancer model. Nanoscale. 2014; 6:15228-35.
31. Liu Q, Zhou M, Li P, Ku G, Huang G, Li C, et al. 64 CuS-labeled nanoparticles: a new sentinel-lymph-node-mapping agent for PET-CT and photoacoustic tomography. Contrast Media Mol Imaging. 2016; 11:475-81.
32. Zhou M, Melancon M, Stafford RJ, Li J, Nick AM, Tian M, et al. Precision Nanomedicine Using Dual Positron Emission Tomography and Magnetic Resonance Temperature Imaging-Guided Photothermal Therapy. J Nucl Med. 2016; 57:1778-83.
33. Zhou M, Zhao J, Tian M, Song S, Zhang R, Gupta S, et al. Radio-photothermal therapy mediated by a single compartment nanoplatform depletes tumor initiating cells and reduces lung metastasis in the orthotopic 4T1 breast tumor model. Nanoscale. 2015; 7:19438-47.
34. Guo L, Yan DD, Yang D, Li Y, Wang X, Zalewski O, et al. Combinatorial photothermal and immuno cancer therapy using chitosan-coated hollow copper sulfide nanoparticles. ACS Nano. 2014; 8:5670-81.
35. Guo L, Panderi I, Yan DD, Szulak K, Li Y, Chen YT, et al. A comparative study of hollow copper sulfide nanoparticles and hollow gold nanospheres on degradability and toxicity. ACS Nano. 2013; 7:8780-93.
36. Wang Z, von dem Bussche A, Kabadi PK, Kane AB, Hurt RH. Biological and environmental transformations of copper-based nanomaterials. ACS Nano. 2013; 7:8715-27.
37. Zhou M, Zhang R, Huang M, Lu W, Song S, Melancon MP, et al. A chelator-free multifunctional [64Cu]CuS nanoparticle platform for simultaneous micro-PET/CT imaging and photothermal ablation therapy. J Am Chem Soc. 2010; 132:15351-8.
38. Garin E, Denizot B, Roux J, Noiret N, Lepareur N, Moreau M, et al. Description and technical pitfalls of a hepatoma model and of intra-arterial injection of radiolabelled lipiodol in the rat. Lab Anim. 2005; 39:314-20.
39. Naito S, von Eschenbach AC, Giavazzi R, Fidler IJ. Growth and metastasis of tumor cells isolated from a human renal cell carcinoma implanted into different organs of nude mice. Cancer Res. 1986; 46:4109-15.
40. Lefevre G, Bessiere J, Ehrhardt JJ, Walcarius A. Immobilization of iodide on copper(I) sulfide minerals. J Environ Radioact. 2003; 70:73-83.
41. Acharya S, Sahoo SK. PLGA nanoparticles containing various anticancer agents and tumour delivery by EPR effect. Adv Drug Deliv Rev. 2011; 63:170-83.
42. Zha Z, Zhang S, Deng Z, Li Y, Li C, Dai Z. Enzyme-responsive copper sulphide nanoparticles for combined photoacoustic imaging, tumor-selective chemotherapy and photothermal therapy. Chem Commun (Camb). 2013; 49:3455-7.
43. Wang Z, Huang P, Jacobson O, Wang Z, Liu Y, Lin L, et al. Biomineralization-Inspired Synthesis of Copper Sulfide-Ferritin Nanocages as Cancer Theranostics. ACS Nano. 2016; 10:3453-60.
44. Avram AM, Esfandiari NH, Wong KK. Preablation 131-I scans with SPECT/CT contribute to thyroid cancer risk stratification and 131-I therapy planning. J Clin Endocrinol Metab. 2015; 100:1895-902.
45. Xi G, Hu X, Wu B, Jiang H, Young CY, Pang Y, et al. Autophagy inhibition promotes paclitaxel-induced apoptosis in cancer cells. Cancer Lett. 2011; 307:141-8.
46. Gao M, Zhang D, Jin Q, Jiang C, Wang C, Li J, et al. Combretastatin-A4 phosphate improves the distribution and antitumor efficacy of albumin-bound paclitaxel in W256 breast carcinoma model. Oncotarget. 2016; 7:58133-41.
47. Cividalli A, Cruciani G, Livdi E, Pasqualetti P, Tirindelli Danesi D. Hyperthermia enhances the response of paclitaxel and radiation in a mouse adenocarcinoma. Int J Radiat Oncol Biol Phys. 1999; 44:407-12.
48. Champion C, Zanotti-Fregonara P, Hindie E. CELLDOSE: a Monte Carlo code to assess electron dose distribution--S values for 131I in spheres of various sizes. J Nucl Med. 2008; 49:151-7.
49. Qian J, Truebenbach J, Graepler F, Pereira P, Huppert P, Eul T, et al. Application of poly-lactide-co-glycolide-microspheres in the transarterial chemoembolization in an animal model of hepatocellular carcinoma. World J Gastroenterol. 2003; 9:94-8.
50. Bastian P, Bartkowski R, Kohler H, Kissel T. Chemo-embolization of experimental liver metastases. Part I: distribution of biodegradable microspheres of different sizes in an animal model for the locoregional therapy. Eur J Pharm Biopharm. 1998; 46:243-54.
51. Lu DS, Raman SS, Vodopich DJ, Wang M, Sayre J, Lassman C. Effect of vessel size on creation of hepatic radiofrequency lesions in pigs: assessment of the "heat sink" effect. AJR Am J Roentgenol. 2002; 178:47-51.
52. Takuma Y, Takabatake H, Morimoto Y, Toshikuni N, Kayahara T, Makino Y, et al. Comparison of combined transcatheter arterial chemoembolization and radiofrequency ablation with surgical resection by using propensity score matching in patients with hepatocellular carcinoma within Milan criteria. Radiology. 2013; 269:927-37.
53. Ni JY, Liu SS, Xu LF, Sun HL, Chen YT. Meta-analysis of radiofrequency ablation in combination with transarterial chemoembolization for hepatocellular carcinoma. World J Gastroenterol. 2013; 19:3872-82.

54. Raoul JL, Sangro B, Forner A, Mazzaferro V, Piscaglia F, Bolondi L, et al. Evolving strategies for the management of intermediate-stage hepatocellular carcinoma: available evidence and expert opinion on the use of transarterial chemoembolization. Cancer Treat Rev. 2011; 37:212-20.
55. Shi Y, Zhai B. A Recent Advance in Image-Guided Locoregional Therapy for Hepatocellular Carcinoma. Gastrointest Tumors. 2016; 3:90-102.
56. Choi JW, Cho HJ, Park JH, Baek SY, Chung JW, Kim DD, et al. Comparison of drug release and pharmacokinetics after transarterial chemoembolization using diverse lipiodol emulsions and drug-eluting beads. PLoS One. 2014; 9(e): 115898.
57. Idee JM, Guiu B. Use of Lipiodol as a drug-delivery system for transcatheter arterial chemoembolization of hepatocellular carcinoma: a review. Crit Rev Oncol Hematol. 2013; 88:530-49.
58. Rognoni C, Ciani O, Sommariva S, Facciorusso A, Tarricone R, Bhoori S, et al. Trans-arterial radioembolization in intermediate-advanced hepatocellular carcinoma: systematic review and meta-analyses. Oncotarget. 2016; 7:72343-55.
59. Salem R, Gordon AC, Mouli S, Hickey R, Kallini J, Gabr A, et al. Y90 Radioembolization Significantly Prolongs Time to Progression Compared With Chemoembolization in Patients With Hepatocellular Carcinoma. Gastroenterology. 2016; 151:1155-63.
60. Sacco R, Conte C, Tumino E, Parisi G, Marceglia S, Metrangolo S, et al. Transarterial radioembolization for hepatocellular carcinoma: a review. J Hepatocell Carcinoma. 2016; 3:25-9.
61. Dhanasekaran R, Kooby DA, Staley CA, Kauh JS, Khanna V, Kim HS. Comparison of conventional transarterial chemoembolization (TACE) and chemoembolization with doxorubicin drug eluting beads (DEB) for unresectable hepatocelluar carcinoma (HCC). J Surg Oncol. 2010; 101:476-80.
62. Lencioni R, de Baere T, Burrel M, Caridi JG, Lammer J, Malagari K, et al. Transcatheter treatment of hepatocellular carcinoma with Doxorubicin-loaded DC Bead (DEBDOX): technical recommendations. Cardiovasc Intervent Radiol. 2012; 35:980-5.
63. Nicolini A, Martinetti L, Crespi S, Maggioni M, Sangiovanni A. Transarterial chemoembolization with epirubicin-eluting beads versus transarterial embolization before liver transplantation for hepatocellular carcinoma. J Vasc Interv Radiol. 2010; 21:327-32.
64. Li X, Feng GS, Zheng CS, Zhuo CK, Liu X. Expression of plasma vascular endothelial growth factor in patients with hepatocellular carcinoma and effect of transcatheter arterial chemoembolization therapy on plasma vascular endothelial growth factor level. World J Gastroenterol. 2004; 10:2878-82.
65. Liang B, Zheng CS, Feng GS, Wu HP, Wang Y, Zhao H, et al. Correlation of hypoxia-inducible factor 1alpha with angiogenesis in liver tumors after transcatheter arterial embolization in an animal model. Cardiovasc Intervent Radiol. 2010; 33:806-12.
66. Chen L, Sun J, Yang X. Radiofrequency ablation-combined multimodel therapies for hepatocellular carcinoma: Current status. Cancer Lett. 2016; 370:78-84.
67. Tacher V, Duran R, Lin M, Sohn JH, Sharma KV, Wang Z, et al. Multimodality Imaging of Ethiodized Oil-loaded Radiopaque Microspheres during Transarterial Embolization of Rabbits with VX2 Liver Tumors. Radiology. 2016; 279:741-53.
68. Oerlemans C, Seevinck PR, Smits ML, Hennink WE, Bakker CJ, van den Bosch MA, et al. Holmium-lipiodol-alginate microspheres for fluoroscopy-guided embolotherapy and multimodality imaging. Int J Pharm. 2015; 482:47-53.
69. Chung EY, Kim HM, Lee GH, Kwak BK, Jung JS, Kuh HJ, et al. Design of deformable chitosan microspheres loaded with superparamagnetic iron oxide nanoparticles for embolotherapy detectable by magnetic resonance imaging. Carbohydr Polym. 2012; 90:1725-31.